Resolution Enhancement with Machine Learning

Ergun Simsek and Emerson K. Cho

University of Maryland Baltimore County, 1000 Hilltop Circle, 21250 Baltimore, MD, United States

ABSTRACT

This numerical study uses machine learning techniques to enhance the resolution of local near-field probing measurements when the probe is larger than the examined device. The research shows that machine learning can achieve a spatial resolution of $\lambda/10$ with a few wavelength-wide probes while keeping the relative error below 3%. It also finds that fully connected neural networks outperform linear regression with limited training data, but linear regression is both sufficient and efficient for larger data sets. These results suggest that similar machine learning methods can improve the resolution of various experimental measurements.

Keywords: Machine learning, resolution, enhancement, Green's functions.

1. INTRODUCTION

Local near-field probing (LNFP) is a technique that allows for the measurement of electric field distributions in microwave and photonic devices, and there are mainly two different variations of it: apertureless[1–5] and aperture-based.[6] In the apertureless method, the probe tip is typically a small metallic tip. When the probe tip is brought close to the device, the electric field induces a shift in the resonance frequency of the probe tip. The electric field distribution can be mapped with high spatial resolution by measuring the frequency shift at various points along the device. In the aperture-based method, the probe tip is a small aperture that allows microwaves to pass through and interact with the device being measured. The electric field is determined by detecting the transmitted or reflected microwave signals. When the probe used in LNFP is smaller than the device being studied, one can successfully measure the electric field distribution along the device.[1–6] However, if the probe is wider than the device, resolution issues arise due to the limitation imposed by the probe size and the distance between the probe and the sample surface.[7]

Various techniques are available to enhance the resolution of LNFP in such contexts. One such technique involves using imaging algorithms to process the data collected by LNFP, thereby aiding in resolution improvement. Deconvolution algorithms,[8–10] for example, can be applied to counteract the effects of probe size and distance from the device. In this research, we employ an alternative method, specifically a machine learning approach, to predict the electric field distribution along a device when the width of a passive electric-field sensing probe surpasses the length of the device under study. Although the device we focus on is a photodetector, the methodologies discussed are general and applicable to any measurement setup.

The structure of this paper is as follows. Initially, we outline a simple numerical model that replicates a typical setup used in LNFP measurements. Subsequently, we apply two machine learning (ML) techniques, namely linear regression and fully connected neural networks (FCNNs), to predict the true electric field profile within the device from synthetic LNFP measurement data for two different scenarios. In the first scenario, all devices examined have a uniform length of 1 μm, and we assess the accuracy and efficiency of the two ML methods based on the size of the training data set. In the second scenario, we evaluate a data set of devices with lengths ranging from 1 μm to 4 μm. Our results demonstrate that with a large data set, linear regression can produce accurate predictions in mere seconds, if not milliseconds, eliminating the need to construct and train a neural network. However, the accuracy of FCNNs remains relatively unaffected by the data set size, making them more precise than linear regression for smaller training data sets.

Further author information: (Send correspondence to E. S.)
E-mail: simsek@umbc.edu, Telephone: 1 410 455 3540

2. A SIMPLE MATHEMATICAL MODEL TO MIMIC LNFP MEASUREMENTS

Figure 1 depicts a simplified setup used in this study to simulate an LNFP measurement configuration. The device being examined, with the goal of measuring the electric field distribution over it via near-field scanning, is centered at the origin with its upper surface at $z = 0$. The width of the device, indicated by the dashed black lines, is w_d. The light gray rectangle signifies the probe, with a width of w_p, where $w_p > w_d$, and x_c denotes the center of the probe. Since our goal is to mimic an LNFP measurement, we can simplify the problem by ignoring the material properties of the probe and approximately calculate the measured field (E_m) using layered medium Green's functions (LMGFs) as follows.

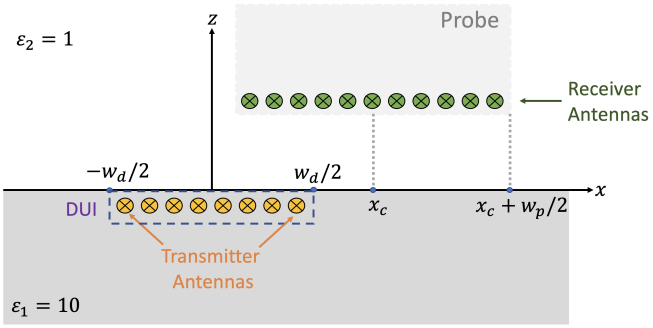

Figure 1. Illustration of the geometry that aims to mimic E-field measurement with a probe over a device.

LMGFs represent the impulse response of a planar multi-layered structure to electrical and magnetic sources.[11] In our implementation, we assume that layer interfaces are parallel to the xy-plane, and layer-i is characterized by its relative electrical permittivity ($\epsilon_{r,i}$), conductivity (σ_i), magnetic relative permeability ($\mu_{r,i}$), and layer thickness (t_i). $G^{EJ}_{\eta\zeta}(x, z|x', z')$ type of LMGFs provide the η-component of the electric field at a target point (x, z) due to a Hertzian dipole antenna located at (x', z') oriented along ζ, where η and ζ can be x, y, or z.[11] Knowing the true electric field distribution (E_r) along the device D, see Fig. 2 (a) as an example, we can assume a finite number of imaginary transmitter antennas placed inside the device, using the local electric field intensity as the current driving them. Similarly, we can assume that the fields generated by these imaginary transmitter antennas can be measured by imaginary receiver antennas within the probe. If the photodetector is excited with y-polarized light, then the electric fields inside the device and measured by the probe are predominantly y-polarized. Hence, we can use G^{EJ}_{yy}-type layered medium Green's functions to approximate E_m using the following expression

$$E_m(x_c, z_r) = \int x_c - w_p/2^{x_c+w_p/2} \int_{-w_d/2}^{w_d/2} E_r(x', z_t) \quad \times G^{EJ}_{yy}(x, z_r|x', z_t)dx'dx, \tag{1}$$

where z_t and z_r are the z-coordinates of the imaginary transmitter and receiver antennas inside the device and probe, respectively.

For our numerical analysis, we chose photodetectors[12–14] as the subject of investigation. By solving the drift-diffusion equations[13] on non-uniform spatial and temporal meshes,[12] using either monochromatic or broadband excitations,[14] we can accurately and efficiently determine both the field and current distributions within the photodetector. Specifically, the non-uniform time-stepping feature allows us to analyze thousands of photodetectors within a few hours using standard personal computers.[15] To create a variety of realistic electric field profiles, we generated 2330 unique modified uni-traveling wave carrier photodetectors by randomly selecting layer thicknesses and doping levels. The number of layers is 16, and the material and doping types are assumed to be the same as those used in.[14] The beam and photodetector diameters are 28 μm, with a continuous laser wavelength of 1550 nm. The modulation frequency (f_{mod}) and modulation depth are 1 GHz and 4%, respectively, i.e., $P_{\text{in}} = P_0 \times [1 + 0.04\cos(2\pi f_{\text{mod}} t)]$, where $P_0 = 1$ mW and t is time. As illustrated in Fig. 2(b), the photodetector is reverse biased at 9 V, and the load resistance is 50 Ω.

To compute the LMGFs, we assume the background consists of two layers: the permittivity of the $z < 0$ region is 10, typical for most semiconductors. The upper layer $z \geq 0$ is air, i.e., $\epsilon_{r,2} = 1$. We assume N_t imaginary

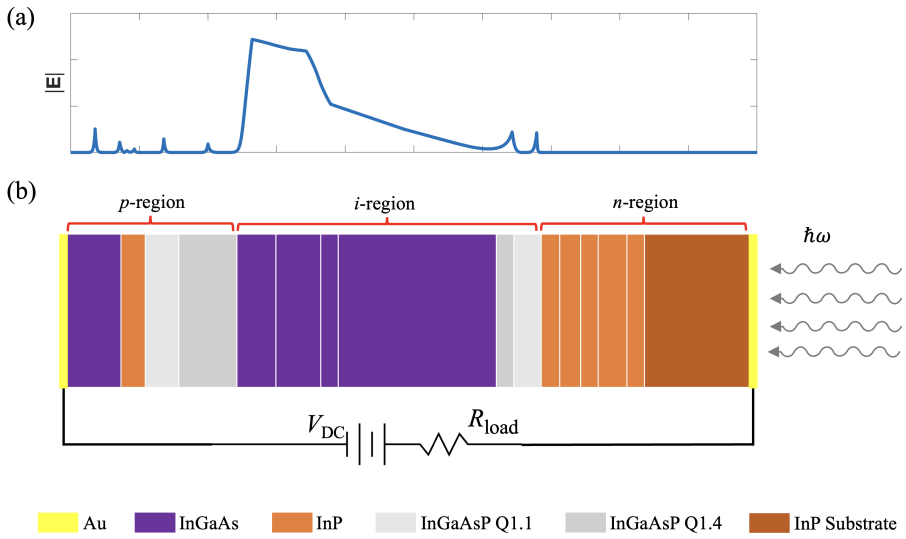

Figure 2. (a) Electric field distribution along the photodetector calculated with the aforementioned drift-diffusion equations solver,[12–15] where the strength is high along the intrinsic (i) region. In this study, we refer to these field profiles as the "true" field profiles. Note the peaks occurring on the interfaces. (b) Schematic illustration of a reverse-biased photodetector that is excited from its n-side. The yellow, purple, orange, light gray, dark gray, and dark orange layers represent Au (contacts), InGaAs, InP, InGaAsP Q1.1, InGaAsP Q1.4 layers, and the InP substrate, respectively.

transmitter antennas at $z_t = -400$ nm, uniformly spaced between $x = -w_d/2$ and $x = w_d/2$. Additionally, we assume N_r imaginary receiver antennas at $z_r = 400$ nm, uniformly spaced between $x = x_c - w_p/2$ and $x_c + w_p/2$, where the probe width, w_p, is 10 μm. Note that these imaginary antennas are infinitesimal ("ideal") dipole antennas, with lengths much smaller than the wavelength. We determine the parameters N_r and N_t so that the inter-antenna spacings, both within the device and probe, are close to $\lambda/20$.

3. NUMERICAL RESULTS

To simplify our analysis, we begin by standardizing the thickness of each layer within the photodetector, ensuring that the total length of each photodetector equals 1 μm, denoted as $w_d = 1$ μm. Employing two machine learning algorithms, namely linear regression (LR) and fully connected neural networks (FCNN), we aim to predict the authentic electric field profiles along the photodetectors based on the electric field profiles obtained from probing measurements. *

Our FCNN architecture is specified as follows: the input comprises blurred electric field measurements, E_m in Eq. (1), while the output corresponds to the true field profile, E_r in Eq. (1). Four hidden layers, each containing 800 neurons, reside between the input and output layers, employing ReLU activation functions. We adopt a learning rate of 10^{-3} and Adamax as the optimizer, with mean squared error defining the loss function. Training spans 200 epochs.

Figure 3 (a) illustrates two exemplary prediction outcomes of the LR model. In both instances, LR accurately identifies the intrinsic layer, characterized by a high electric field strength ($|\mathbf{E}|$), and estimates the maximum value of $|\mathbf{E}|$, providing a rough depiction of its variation within the intrinsic region. Despite occasional negative predictions, which deviate from physical expectations, LR remains a useful tool for approximating $|\mathbf{E}|$, given its swift prediction capability, taking merely milliseconds to compute. Figure 3 (b) showcases two sample prediction results from the FCNN model. Once again, accurate predictions of the intrinsic region's location and $|\mathbf{E}|$ maximum are observed, without any negative predictions. However, training the neural network necessitates a longer duration, approximately a minute for 200 epochs, compared to LR. The average relative error for both

*Access to both the datasets and the codes used for generating these results is available at https://github.com/simsekergun/Resolution

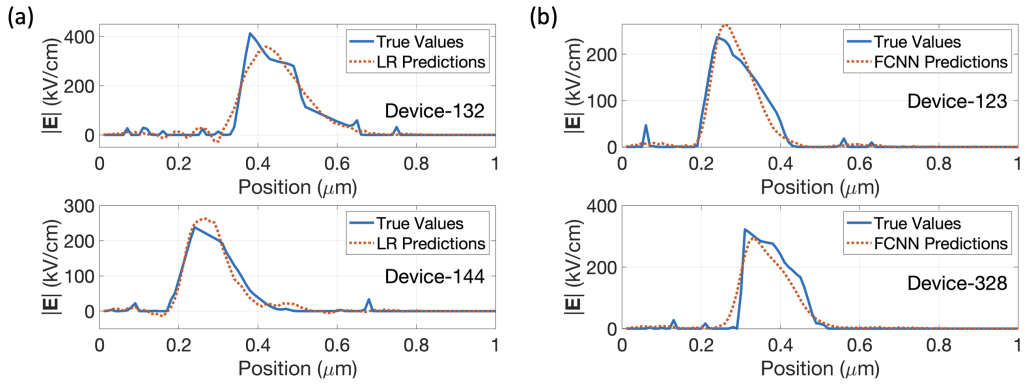

Figure 3. Electric field profiles: truth (blue solid curves) vs. prediction (red dashed curves) obtained with (a) the linear regression model and (b) FCNN for two randomly selected photodetectors.

approaches, defined as the absolute difference between the true (E_{true}) and predicted (E_{pred}) values divided by $E_{\text{true}} + \xi$, where ξ is a small positive number to prevent division by zero errors, remains close to $0.03 \pm 0.01\%$, with a maximum relative error of 2.5 ± 0.3

In the results depicted in Figure 3, 80% of the data was allocated for training, while the remaining 20% was designated for testing. To explore the impact of training data set size (N_{training}) on accuracy, additional predictions were conducted by varying N_{training} from 10 to 1600. Figure 4 (a) illustrates how the normalized mean squared error changes with N_{training}. Notably, the FCNN's accuracy remains nearly independent of N_{training} for $N_{\text{training}} \geq 100$, while the LR model exhibits significant errors for small N_{training} cases ($N_{\text{training}} < 200$). This discrepancy arises from the equal influence each sample holds over LR predictions, making inaccurate predictions more likely, especially when correlations between training and test data sets are low or when the training data set comprises samples markedly different from those in the testing data set.

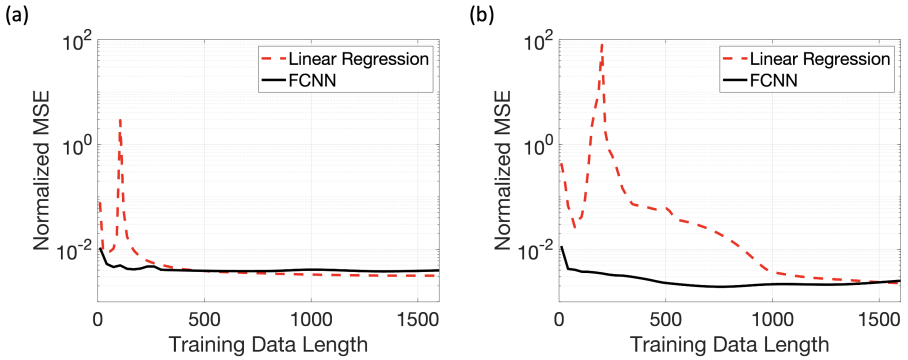

Figure 4. Normalized mean squared error as a function of training data set size for linear regression (blue solid curve) and an FCNN (red dotted curve) for a data set with devices of (a) constant length and (b) varying length.

In the second scenario, we investigate photodetectors with original lengths ranging from 1 μm to 4 μm, i.e., $1\ \mu\text{m} \leq w_d \leq 4\ \mu\text{m}$. Employing the same machine learning models, we find that with 80% of the data for training, highly accurate predictions are achievable. However, as illustrated in Fig. 4 (b), the accuracy of LR is significantly influenced by N_{training}. This dependency underscores that lacking similar samples in the training data set relative to the testing data set can compromise the LR models' accuracy. Conversely, akin to the analysis with constant device length, the FCNN's accuracy remains largely unaffected by N_{training}, owing to its multiple layers and hundreds of neurons, facilitating effective learning of underlying patterns even from small training data sets.

4. CONCLUSION

In this work, we have examined the application of machine learning methods to improve the resolution of local near-field probing measurements, especially when the probe size exceeds that of the device under examination. The outcomes reveal three primary discoveries: (i) leveraging machine learning enables achieving a spatial resolution of $\lambda/10$ even with probes that are only a few λ wide, while maintaining a maximum relative error below 3%; (ii) fully connected neural networks outperform linear regression models in accuracy when dealing with limited training data sets; and (iii) for extensive training data sets, constructing and training a neural network is unnecessary as linear regression proves to be both adequate and efficient. These findings suggest the potential application of similar machine learning techniques to enhance resolution in diverse measurement setups.

REFERENCES

[1] Dutta, S. K., Vlahacos, C. P., Steinhauer, D. E., Thanawalla, A. S., Feenstra, B. J., Wellstood, F. C., Anlage, S. M., and Newman, H. S., "Imaging microwave electric fields using a near-field scanning microwave microscope," *Applied Physics Letters* **74**, 156–158 (Jan. 1999).

[2] Kantor, R. and Shvets, I., "Measurement of electric-field intensities using scanning near-field microwave microscopy," *IEEE Transactions on Microwave Theory and Techniques* **51**(11), 2228–2234 (2003).

[3] Dehghan, N., Cripps, S., Porch, A., and Lees, J., "An improved electric field probe with applications in high efficiency PA design and diagnostics," in [*81st ARFTG Microwave Measurement Conference*], 1–4 (2013).

[4] Farina, M., Mencarelli, D., Di Donato, A., Venanzoni, G., and Morini, A., "Calibration protocol for broadband near-field microwave microscopy," *IEEE Transactions on Microwave Theory and Techniques* **59**(10), 2769–2776 (2011).

[5] Hou, R., Lorenzini, M., Spirito, M., Roedle, T., van Rijs, F., and de Vreede, L. C. N., "Nonintrusive near-field characterization of spatially distributed effects in large-periphery high-power GaN HEMTs," *IEEE Transactions on Microwave Theory and Techniques* **64**(11), 4048–4062 (2016).

[6] Pohl, D., Novotny, L., Hecht, B., and Heinzelmann, H., "Radiation coupling and image formation in scanning near-field optical microscopy," *Thin Solid Films* **273**(1), 161–167 (1996). International Symposium on Ultra Materials for Picotransfer.

[7] Cho, E. K. and Simsek, E., "Enhancing the resolution of local near-field probing measurements with machine learning," *IEEE Transactions on Microwave Theory and Techniques* **72**(3), 1515–1519 (2024).

[8] Higgins, P. D., Sibata, C. H., Siskind, L., and Sohn, J. W., "Deconvolution of detector size effect for small field measurement," *Medical Physics* **22**(10), 1663–1666 (1995).

[9] Alda, J., Fumeaux, C., Codreanu, I., Schaefer, J. A., and Boreman, G. D., "Deconvolution method for two-dimensional spatial-response mapping of lithographic infrared antennas," *Applied Optics* **38**(19), 3993–4000 (1999).

[10] Lecaque, R., Grésillon, S., and Boccara, C., "THz emission microscopy with sub-wavelength broadband source," *Opt. Express* **16**, 4731–4738 (Mar 2008).

[11] Simsek, E., Liu, Q. H., and Wei, B., "Singularity subtraction for evaluation of Green's functions for multilayer media," *IEEE Transactions on Microwave Theory and Techniques* **54**(1), 216–225 (2006).

[12] Simsek, E., Anjum, I. M., Carruthers, T. F., and Menyuk, C. R., "Non-uniform time-stepping for fast simulation of photodetectors under high-peak-power, ultra-short optical pulses," in [*2022 International Conference on Numerical Simulation of Optoelectronic Devices (NUSOD)*], IEEE (sep 2022).

[13] Simsek, E., Anjum, I. M., and Menyuk, C. R., "Solving drift diffusion equations on non-uniform spatial and temporal domains," in [*2023 Photonics & Electromagnetics Research Symposium (PIERS)*], 1644–1651 (2023).

[14] Simsek, E., Anjum, I. M., Carruthers, T. F., Menyuk, C. R., Campbell, J. C., Tulchinsky, D. A., and Williams, K. J., "Fast evaluation of RF power spectrum of photodetectors with windowing functions," *IEEE Transactions on Electron Devices* **70**, 3643–3648 (July 2023).

[15] Anjum, I. M., Simsek, E., Mahabadi, S. E. J., Carruthers, T. F., Menyuk, C. R., Campbell, J. C., Tulchinsky, D. A., and Williams, K. J., "Use of evolutionary optimization algorithms for the design and analysis of low bias, low phase noise photodetectors," *Journal of Lightwave Technology* **41**, 7285–7291 (Dec. 2023).